

Featuring work from Prof. Siva Vanapalli's microfluidics and cancer research group at Texas Tech University.

Label-free, high-throughput holographic screening and enumeration of tumor cells in blood

A high throughput technology involving microfluidics, digital holography microscopy and machine learning has been developed to detect cancer cells in blood. This label-free approach can enable rapid analysis of liquid biopsy samples in cancer patients.

As featured in:



See Siva A. Vanapalli et al.,
Lab Chip, 2017, 17, 2920.



Cite this: *Lab Chip*, 2017, 17, 2920

Label-free, high-throughput holographic screening and enumeration of tumor cells in blood†

Dhananjay Kumar Singh,  ‡ Caroline C. Ahrens,  ‡ Wei Li  and Siva A. Vanapalli  *

We introduce inline digital holographic microscopy (in-line DHM) as a label-free technique for detecting tumor cells in blood. The optimized DHM platform fingerprints every cell flowing through a microchannel at 10 000 cells per second, based on three features – size, maximum intensity and mean intensity. To identify tumor cells in a background of blood cells, we developed robust gating criteria using machine-learning approaches. We established classifiers from the features extracted from 100 000-cell training sets consisting of red blood cells, peripheral blood mononuclear cells and tumor cell lines. The optimized classifier was then applied to targeted features of a single cell in a mixed cell population to make quantitative cell-type predictions. We tested our classification system with tumor cells spiked at different levels into a background of lysed blood that contained predominantly peripheral blood mononuclear cells. Results show that our holographic screening method can readily detect as few as 10 tumor cells per mL, and can identify tumor cells at a false positive rate of at most 0.001%. This purely optical approach obviates the need for antibody labeling and allows large volumes of sample to be quickly processed. Moreover, our in-line DHM approach can be combined with existing circulation tumor cell enrichment strategies, making it a promising tool for label-free analysis of liquid-biopsy samples.

Received 13th February 2017,
Accepted 7th July 2017

DOI: 10.1039/c7lc00149e

rsc.li/loc

1. Introduction

Circulating tumor cells (CTCs) have been identified in the blood of cancer patients as those cells that have left primary or even metastatic tumors and entered into peripheral blood. As part of so-called liquid biopsies,¹ identifying the presence and assessing the character of CTCs has shown great utility for improving patient care including enabling early cancer detection, determining patient prognosis, and directing longitudinal treatments.^{2–4} Clinical success has motivated the development of a variety of technologies to identify, isolate, and characterize the extremely rare subpopulation of CTCs in patient blood (approximately 1–10 CTCs in 1 billion blood cells).⁵

Established methods for CTC characterization largely rely on differences in biochemical and physical properties between CTCs and blood cells to recover a population enriched in CTCs.⁵ Biochemical techniques typically involve the selective arrest of tumor cells through surface binding of proteins preferentially expressed on the tumor cell surface.⁵ In physical separation approaches, the larger average size of tumor cells compared to blood cells and their distinct viscoelastic

properties⁶ allow for CTC isolation using various filtration and inertial separation techniques.³ Following CTC enrichment, additional characterization, most often *via* immunofluorescence, is used to identify CTCs among contaminating blood cells.⁵ This subsequent processing is necessary to allow accurate CTC enumeration and is useful in identifying and isolating a pure CTC population appropriate for genomic, proteomic, or phenotypic assays.^{5,7}

As the field of CTC isolation and characterization continues to develop, traditional techniques involving selective enrichment followed by label-based CTC identification have become increasingly limiting. Labeling molecules including antibodies used in immunofluorescent staining must be validated for each population with varied resolution dependent on label selection.⁸ Further, while select immunofluorescence detection strategies preserve cell viability,⁹ fixation and permeabilization remain standard for antibody-based characterization.^{7,10} This destructive processing improves cell retention and stability but eliminates the potential for subsequent phenotypic assays. A more optimal characterization technique would be label free, high-throughput and platform flexible.¹¹ Most importantly, the approach should be non-destructive, allowing the recovery of both viable tumor cells and even tumor cell clusters¹² for further downstream processing. Such a technique might be integrated into existing CTC isolation strategies or serve as a stand-alone method for CTC detection.

Department of Chemical Engineering, Texas Tech University, Lubbock, Texas, USA. E-mail: siva.vanapalli@ttu.edu

† Electronic supplementary information (ESI) available. See DOI: 10.1039/c7lc00149e

‡ Equal author contribution.

Several cell characterization technologies have begun to meet these demands for alternative detection. Most common are inertial methods introduced above in which cells are flowed through highly structured microfluidic chips. Differences in size and deformability between tumor cells and blood cells in flow are used to isolate a cell population enriched in CTCs.¹³ However, the overlapping physical properties of the cell types limit recovered cell purity, requiring secondary processing.^{7,10,14} Proof-of-concept studies identified CTCs in a single metastatic prostate cancer patient based on cell passage time through a constriction and buoyant mass, however this developing approach has limited throughput ($\sim 45 \mu\text{L h}^{-1}$) and imperfect resolution, detecting spiked cells with a true positive rate of less than 0.7 even with stringent gating.¹⁵ Label-free Raman spectroscopy is an optical technique used to differentiate tumor cells from blood cells based on inherent differences in amino acid and lipid compositions in the two cell populations,¹⁶ but the label-free technique has limited throughput with demonstrated characterization of less than 500 cells. Other strategies include so-called dielectrophoresis¹⁷ and acoustophoresis,¹⁸ in which electrical and acoustic forces, respectively, have been integrated into microfluidic devices to direct label-free cell separation. These separations are broadly based on a variety of factors including difference in cell size, density, mass, compressibility, shape, and, in the case of dielectrophoresis, electrical properties, but both methods have limited throughput and purity.

Here we introduce inline digital holography microscopy (inline-DHM) as a promising optical, label-free technique for tumor cell identification in mixed samples. In DHM, the interference pattern (hologram) in an image contains information not only about the cells that are in focus but also cells that are out-of-focus.^{19–27} Using diffraction theories, numerical reconstruction is pursued to obtain the in-focus image of every cell in the 3D volume. Because mechanical scanning across sample depth is not needed, holograms can be acquired at much faster rates using high-speed cameras, making the method suitable for large-scale single cell phenotyping. We recently optimized the in-line DHM set up and demonstrated the label-free fingerprinting of thousands of tumor cells in bulk flow.²⁸

Building on these capabilities of DHM, the main challenge we seek to address here is how to identify rare cancer cells that are present in a mixed population of other cells. We exploit both the size and optical characteristics of different cell types to enumerate tumor cells spiked in blood. Training sets of red blood cells (RBCs), peripheral blood mononuclear cells (PBMCs) and tumor cell lines are used to establish rigorous single- and multi-dimensional gating strategies for cell identification with a focus on limiting false positives. These optimized selection criteria are applied to identify tumor cells spiked into lysed whole blood based on key physical differences between the blood and tumor cell types.

2. Results

2.1 Basic principle of inline-DHM for characterizing cells in bulk flow

This section presents the basic principles of recording and reconstruction of optical signatures from cells in bulk flow using inline-DHM. Fig. 1A shows the experimental arrangement of inline-DHM. In brief, the sample volume containing flowing cells in a transparent microchannel is illuminated by a collimated beam of laser light. The forward scattered light from cells and un-scattered light interfere and generate a 2D hologram. The interference pattern is magnified by a microscope objective and imaged onto a CCD sensor. Fig. 1B shows a portion of hologram from MCF7 cells flowing in a rectangular PDMS channel.

The numerical reconstruction of the 2D hologram provides the focused images of cells in the full volume. The size and intensity distributions of the focused image can be obtained numerically. The intensity distribution across the focused image manifests the recorded intensity in the form of a hologram. Fig. 1C shows the plane-wise 3D numerical reconstruction carried out in the full sample volume from the 2D digital hologram shown in Fig. 1B. The reconstruction is performed using the angular spectrum method^{29–31} where the gradient of intensity³² of the cell image along z -direction inside the reconstruction volume indicates the plane of best focus of each cell image. The focused image provides the size and intensity distributions. Fig. 1D shows a representative focused image of a single MCF7 cell and Fig. 1E shows the intensity distribution along the line passing through the center of this image. Detailed reconstruction methodology for characterization of particles^{20,21,23–25,33–36} and of cells including how we eliminate multiple counting of cells from successive images is described in our previous work.²⁸

From the focused image we extract three metrics quantifying the cell size and image intensity. As established in our previous work, the size of the bead or cell is determined using the lateral intensity profile along the line passing through the center of the focused image. The distance between two minima about the central maxima provides the diameter of the bead or cell. Importantly, as shown in Fig. 1E, two optical metrics I_{max} and I_{mean} further characterize the cell. Here I_{max} is the intensity of the single brightest pixel ($2 \times 2 \mu\text{m}^2$) within a given cell image, and I_{mean} is the average intensity of the $6 \times 6 \mu\text{m}^2$ region centered around the most intense pixel. We note that we have mapped the size and pixel values of maximum and mean intensity of focused images of cells on a single plane perpendicular to the direction of light *i.e.* the lateral component of D and I . We have chosen this plane for analysis, because in the longitudinal plane the image of cell is elliptical due to the diffraction limited digital holographic imaging, which might lead to larger errors.

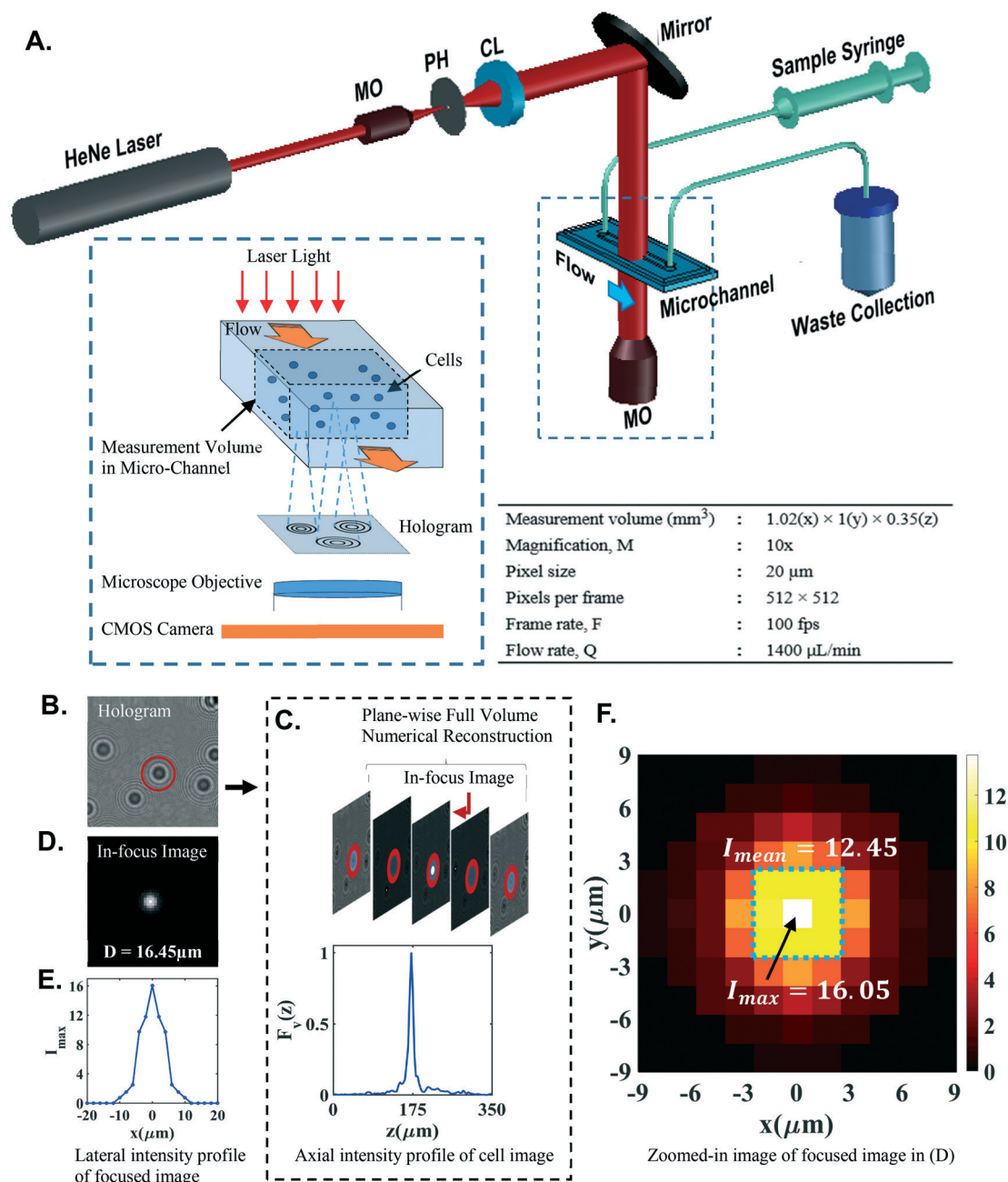


Fig. 1 Principle of inline digital holography microscopy (DHM) for characterizing cells in flow. (A) Shows the experimental arrangement of inline-DHM for recording holograms of cells in bulk flow and the experimental parameters used in this study. Here MO: microscope objective, PH: pin-hole, CL: collimating lens, (B) shows the hologram cropped from the original hologram of MCF7 cells, (C) shows the three-dimensional numerical reconstruction to generate the focused image of cells in the 3D volume, a 2D in-focus image corresponding to the hologram pattern encircled in (B) and the z -location of the focussed image shown by the profile of the gradient of intensity along the z -direction, (D) shows a representative in-focus image of a single MCF7 cell, (E) shows the intensity profile along a line passing through the centre of the in-focus image on the xy -plane, and (F) is a heat map of (D). The maximum intensity (I_{max}) corresponding to the single brightest pixel is indicated with an arrow and the perimeter of the region of mean intensity (I_{mean}) corresponding to $6 \times 6 \mu\text{m}^2$ is indicated by a dashed area.

2.2 Establishing size and optical signatures for single cell characterization

Label-free, high throughput tumor cell enumeration *via* inline-DHM relies on precise and accurate characterization of the size and optical properties of cells flowing through the chosen geometry. In this section, we characterize beads of

known character flowing through a straight rectangular PDMS channel to systematically establish the accuracy and precision of inline-DHM recorded particle size and optical properties. We chose cell-sized beads having varied refractive indexes to establish three distinct metrics, size (D) and maximum (I_{max}) and mean (I_{mean}) intensities. Finally, we explore the interdependence of these metrics and suggest their

additive utility when characterizing both beads and cells. We note that we have limited the overall influence of bead or cell overlap by selecting a seeding density such that the shadow density is less than 5% so that the beads or cells are sparse enough not to overlap significantly on the hologram.^{33–35,37}

We first quantify bead diameters, confirming the accuracy and precision of high throughput inline-DHM based imaging of particles in a 1 mm × 350 μm rectangular PDMS channel. The channel width of 1 mm was chosen as it was the maximum we could accommodate with our camera sensor and the 10× microscope objective magnification that was sufficient to resolve the size of cells. The height of 350 μm was dictated by the constraints of soft lithography used to make the channel and the optimal DHM recording z-distance needed to minimize the error in determining the axial position of beads or cells in the image volume.^{28,33–35,37}

The manufacturer and DHM data for cell-sized (nominal 8 and 15 μm) polystyrene (PS) and silica (SILICA) beads were compared. Bead average diameters and variances of all four bead types, as quantified by DHM, closely match those reported by the manufacturer (Table 1). Further we observed no statistically significant positional variance in diameter measurements (data not shown) confirming our previously published work which established both accurate and precise particle size measurements throughout this depth of flow.²⁸

We next introduce the two optical metrics, I_{\max} and I_{mean} and explore their dependencies on both bead size and inherent optical properties. In the present study, the holograms are generated using the forward scattered light from the beads or cells. A study characterizing beads suspended in water found that $S = 0.15D^3$ and $0.29D^{3.3}$ for beads having refractive indices 1.59 and 1.40 respectively, where S is the forward scattering intensity collected within a 2° angle and D is the diameter of the beads.³⁸ Thus, the forward scattered light predominantly depends on the size of the beads and increases with the increase in bead diameter and decreases with the increase in the bead refractive index. These previous findings support that the forward scattered light contains the information of size and refractive index of a particle but, predominantly, depends on the particle size.

Experimentally observed values of I_{\max} and I_{mean} for the four bead populations generally follow expected trends (Table 1). Considering first I_{\max} , the average recorded intensities for the four bead types range from 0.86 to 4.68 (Table 1). We find I_{\max} is higher for beads having the same diameter but lower refrac-

tive index, and is higher for larger beads with the same refractive index (Table 1). The second intensity metric, I_{mean} , follows similar dependencies on bead size and refractive index as does I_{\max} . However, for all bead populations the average values and coefficients of variance (CV) of I_{mean} are less than those of I_{\max} as I_{mean} is calculated from the average intensities of the I_{\max} pixel and the surrounding eight pixels.

The observed close correlation between the two optical signatures, I_{\max} and I_{mean} is expected for homogeneous particles having uniform refractive indexes. However, unlike beads, cells have greater internal complexities and local variations of optical properties. For example, in live HeLa cells, an ovarian cancer cell line, the refractive indices of the nucleus, nucleolus and cytosol have been measured using tomographic phase imaging to be 1.355–1.365 RIU, 1.375–1.385 RIU, and 1.36–1.39 RIU, respectively.³⁹ Considering applications focused on identifying tumor cells in blood, it is useful to also consider those of lymphocytes and monocytes, two populations of white blood cells. Based on light scattering and multiple-layer spherical models lymphocytes were found to have a nuclear and cytoplasmic refractive index of 1.43 ± 0.05 RIU and 1.356 ± 0.009 RIU, respectively; whereas monocytes were found to have a nuclear and cytoplasmic refractive index of 1.43 ± 0.04 RIU and 1.348 ± 0.004 RIU, respectively.⁴⁰ The above analysis indicates that for same size of cells their internal complexities may differ from each other which in turn may affect the scattered light from cells. For tumor and white blood cells, I_{\max} represents the maximum intensity corresponding to the single bright pixel at the core of a focused image hence is primarily affected by the size of the cell due to forward scattering; whereas I_{mean} , a 3×3 pixel² region of the focused image, is expected to be influenced by the optical properties of a region extending throughout both the nucleus and regions of the cytoplasm.

To further explore the dependencies in cells among the three metrics, D , I_{\max} , and I_{mean} , 100 000 cells from each of the three cell populations were characterized. Specifically, we characterized PBMCs isolated from donor blood through red blood cell lysis and two breast cancer cell lines (MDA-MB-231 and MCF7). Scatter plots suggest a strong relationship between I_{mean} and I_{\max} with a covariance quantified as 0.46, 0.87, and 0.79 for PBMC, MDA-MB-213 and MCF7 cells, respectively (Fig. 2A–C). That these correlation coefficients are not closer to 1 support the non-redundant nature of these two intensity metrics in characterizing cells. Further, the correlation coefficients between D and I_{\max} (Fig. 2D–F) as well as

Table 1 The distribution [$\mu \pm \text{CV}(\%)$] of diameter (D), maximum intensity (I_{\max}), and mean intensity (I_{mean}), of polystyrene (PS) and silica (SILICA) beads obtained from inline-DHM. The data was generated from atleast 100 000 particles for each bead type

Bead type	Manufacturer data		DHM data		
	D	RI	D	I_{\max}	I_{mean}
Polystyrene	8.23 μm ± 6%	1.59	8.32 μm ± 9%	0.86 ± 25%	0.37 ± 20%
SILICA	8.32 μm ± 6%	1.4	8.39 μm ± 9%	1.68 ± 25%	0.47 ± 20%
Polystyrene	15.13 μm ± 6%	1.59	15.14 μm ± 3%	2.41 ± 32%	0.49 ± 24%
SILICA	15.14 μm ± 3%	1.4	15.32 μm ± 4%	4.68 ± 32%	0.91 ± 24%

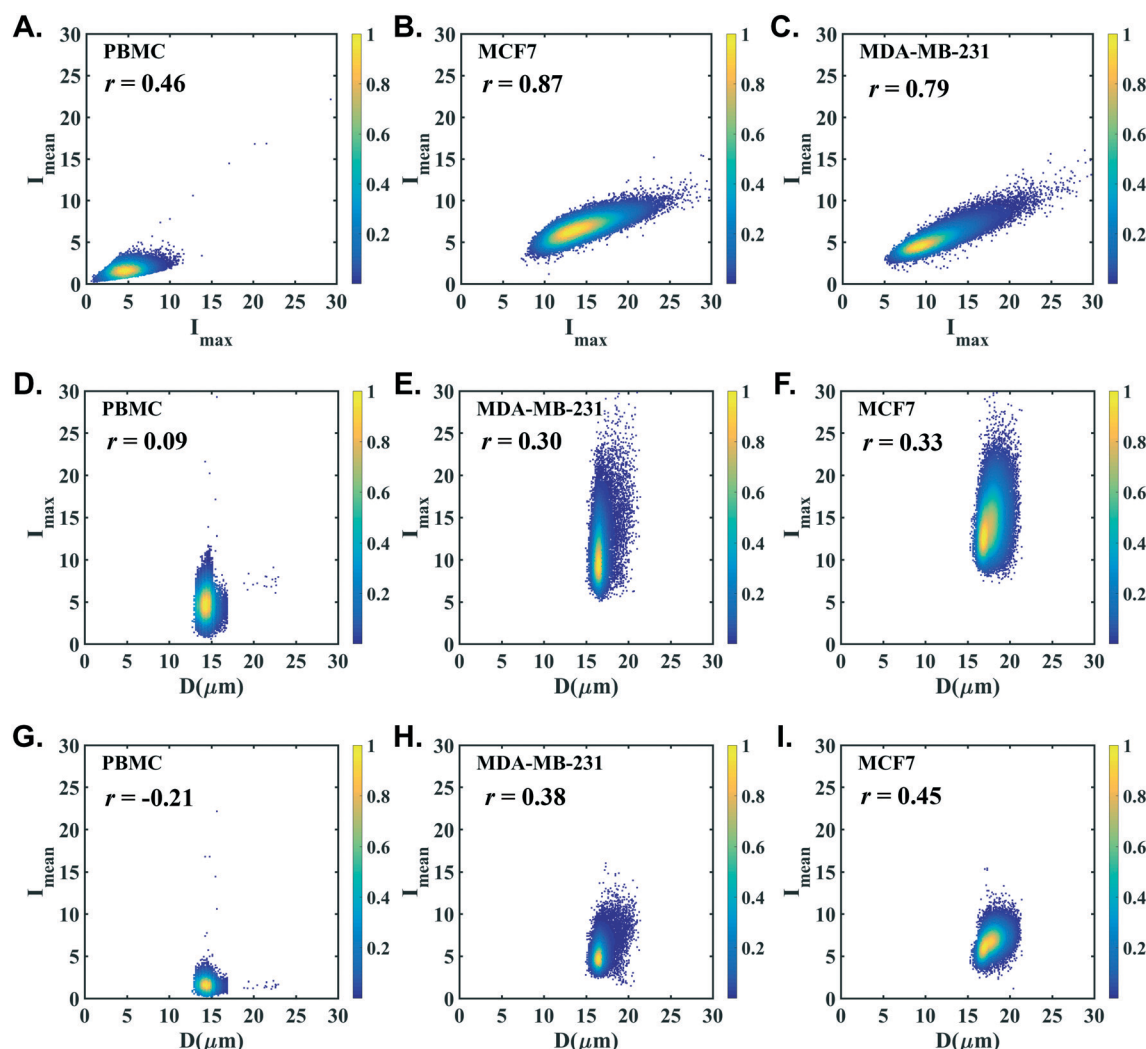


Fig. 2 Binary correlations between the three metrics of size (D), maximum (I_{\max}) and mean (I_{mean}) intensity for PBMCs (A, D, and G) and two cancer cell lines, MDA-MB-231 (B, E, and H) and MCF-7 (C, F, and I). Cell types and the correlation coefficient (r) between the metrics are shown as an inset. The number of cells analyzed to generate each plot is 100 000. Scale bar shows the normalized density distribution.

D and I_{mean} (Fig. 2G–I) are less than 0.5 for all cell three cell populations and is not increased when comparing with D^3 , further supporting that our optical signatures are not exclusively dictated by cell size.

In summary, inline-DHM characterization in bulk flow of beads having known sizes and optical properties supports the three metrics, size (D), maximum intensity (I_{\max}) and mean intensity (I_{mean}), as robust measures for use in cell discrimination and classification. Further, our results establish the practical utility of the two metrics of scattered intensity, I_{\max} and I_{mean} , as complementary to and non-redundant with size-based inline-DHM cell characterization.

2.3 Establishing optimized classifiers for identifying targeted cells

This work focuses on method development that might be readily extended to detecting tumor cells in patient blood. Here, MDA-MB-231 and MCF7 breast cancer cell lines act as

models for patient-derived CTCs. Like CTCs, these cell lines have similarly increased average sizes and refractive indices compared to blood-derived cells.^{41,42} Although we anticipate applications using inline-DHM to quantify tumor-like cells in patient whole blood, this work focuses on identifying tumor cells among the PBMC sub-fraction of healthy donor blood. A background of the red blood cell lysis derived PBMC sub-population was chosen for preliminary experiments rather than whole blood to allow rapid development of metrics differentiating tumor cells from normal blood while minimizing computational processing required to characterize large numbers of readily differentiated red blood cells.

Fig. 3 shows the workflow that we used, which is well established within the field of machine learning to develop classifiers from features extracted from the simplified training sets. We used single populations of blood cells including RBCs and PBMCs isolated from donor blood through red blood cell lysis as well as of two breast cancer cell lines (MDA-MB-231 and MCF7) as training sets. Optimized

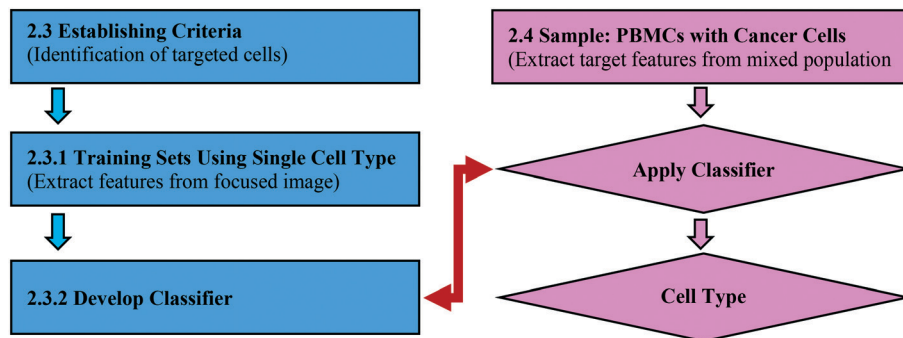


Fig. 3 Data analysis workflow to develop classifier and detection of tumor cells.

classifiers were then applied to identify cancer cell lines within a background of blood cells.

2.3.1 Training sets using single cell types: characteristic features. We extracted the characteristic features of cells from the numerical reconstruction of digital holograms of single populations of blood cells including RBCs, PBMCs and the two cancer cell lines (MDA-MB-231 and MCF7). For each sub-population, the three metrics: D , I_{\max} and I_{mean} were recorded from 100 000 flowing cells. The average diameters of the cell populations closely follow expected values (Fig. 4A). Literature suggests that the mean diameter across the long axis of disk-like red blood cells is around $8\text{ }\mu\text{m}$ compared to the DHM-recorded average diameter of $7.6\text{ }\mu\text{m}$. Of note, the $10\times$ magnification employed here generates a 3 to 4 pixel reconstructed image for each RBC making the optical resolution and intensity based characterization insufficient to resolve the asymmetric character of RBCs as the size of each pixel is $2 \times 2\text{ }\mu\text{m}^2$. The mean size of PBMCs is reported to be around $14\text{ }\mu\text{m}$ (ref. 43) closely matching the recorded cell diameter of $14.12\text{ }\mu\text{m}$. Similarly, reported tumor cell diameters fall between 15 and $20\text{ }\mu\text{m}$ (ref. 44) compared to recorded average diameters of $16.61\text{ }\mu\text{m}$ and $17.87\text{ }\mu\text{m}$ for MDA-MB-231 and MCF7 cells, respectively.

As established in the previous section, intensity metrics are expected to incorporate aspects of both the cell size and optical properties. Comparing the average value mean (I_{mean})

and maximum (I_{\max}) intensities indicates the strong correlation of cell size with observed intensities. Broadly, the rank order of cell types by increasing diameter mirrors that by both I_{\max} and I_{mean} (Fig. 4).

Finally, comparing the overall probability densities with respect to diameter, I_{mean} and I_{\max} from pure population of RBCs, PBMCs, MDA-MB-231 and MCF7 supports red blood cells having much smaller average diameters might be readily distinguished from PBMCs and both cancer cell lines. However, it is clear from Fig. 4 that, as would also be expected for patient derived samples, the individual intensity and diameter distributions of the PBMCs and tumor cells are not discrete. The overlapping individual metrics demand further optimization of classification strategies, including those incorporating intensity metrics, to achieve robust cell identification.

2.3.2 Developing classifier. The training sets of known cell populations can be used to train classifiers able to identify cells within mixed populations. Each classification strategy balances the tolerance for false positives, the tolerance for false negatives, and computational simplicity where the optimal process is dependent on the end application. For example, screening for CTCs in dilute blood might require an extremely low tolerance for false positives (*i.e.* blood cells identified as tumor cells) as the great excess of blood cells compared to tumor cells would lead both healthy and normal

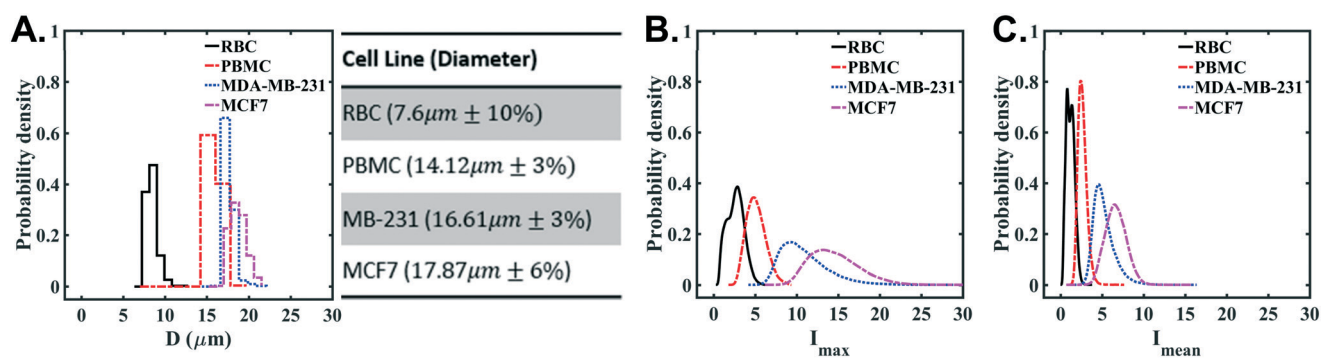


Fig. 4 Characteristic features of pure populations of different cell types. Probability density with respect to (A) diameter, D , (B) maximum intensity, I_{\max} , and (C) mean intensity, I_{mean} , of different types of pure cellular populations. The data was generated from at least 100 000 cells of RBCs, PBMCs, MDA-MB-231 cells, and MCF7 cells.

patients to have a large number of cells classified as tumor cells. Screening on subpopulations enriched in CTCs might favor classification strategies with limited false negatives. In all cases, incorporating multiplexed metrics has the potential to increase overall accuracy, but also risks overfitting the system and unnecessarily complicating downstream processing.

We first quantify the capabilities of the simple classification strategy, binary classifiers, for differentiating targeted tumors cells among a background of PBMCs. To visualize the classification accuracy, we use a receiver operating characteristic (ROC) curve which is generated by plotting the true positive rate (TPR) and false positive rate (FPR) at various threshold settings. Fig. 5A and B show the ROC curve visually demonstrating the accuracy of each of the three metrics, D , I_{\max} , and I_{mean} in differentiating PBMCs from each of the cancer cell lines (MDA-MB-231 and MCF7). Fig. 5C and D are zoomed in presentations corresponding to Fig. 5A and B respectively for visual clarity. From these figures, it is clear that the area under the curve (AUC) is more than 0.9 for all three characteristic curves of D , I_{\max} , and I_{mean} for both the populations PBMC & MDA-MB-231 and PBMC & MCF7. This indicates that while diameter is the most robust independent discriminating metric, all three metrics can be used as strong

classifiers to identify tumor cells in a lysed blood population of PBMCs with a high TPR and with a very low FPR.

Applications requiring more resolved separations are expected to benefit from more developed gating strategies integrating multiple classifiers. Fig. 6 shows one such approach, the decision tree based on the CART-algorithm, to develop a classifier from the pure subpopulations of PBMC & MDA-MB-231 (Fig. 6A) and PBMC & MCF7 (Fig. 6C), respectively. The maximum split limit has been set as 6 for both cases. At every branching point of the tree, the twoing method is used to optimize the classifier among three characteristic metrics D , I_{\max} , and I_{mean} . Fig. 6B shows that 124 957 MDA-MB-231 cells out of 125 000 cells within the training set were predicted as true positive and with 0 false positives from 150 000 cells of PBMCs. Similarly, Fig. 6D shows that 124 957 MCF7 cells out of 125 000 cells were predicted as true positives and with only one false positive from the population of 150 000 PBMCs. It can be concluded that the present machine learning algorithm provides high accuracy identifying targeted cells based on their three characteristics, D , I_{\max} , and I_{mean} . As expected from single cell metrics, diameter is the overriding discriminating metric for both decision trees; however, incorporating data from both intensity

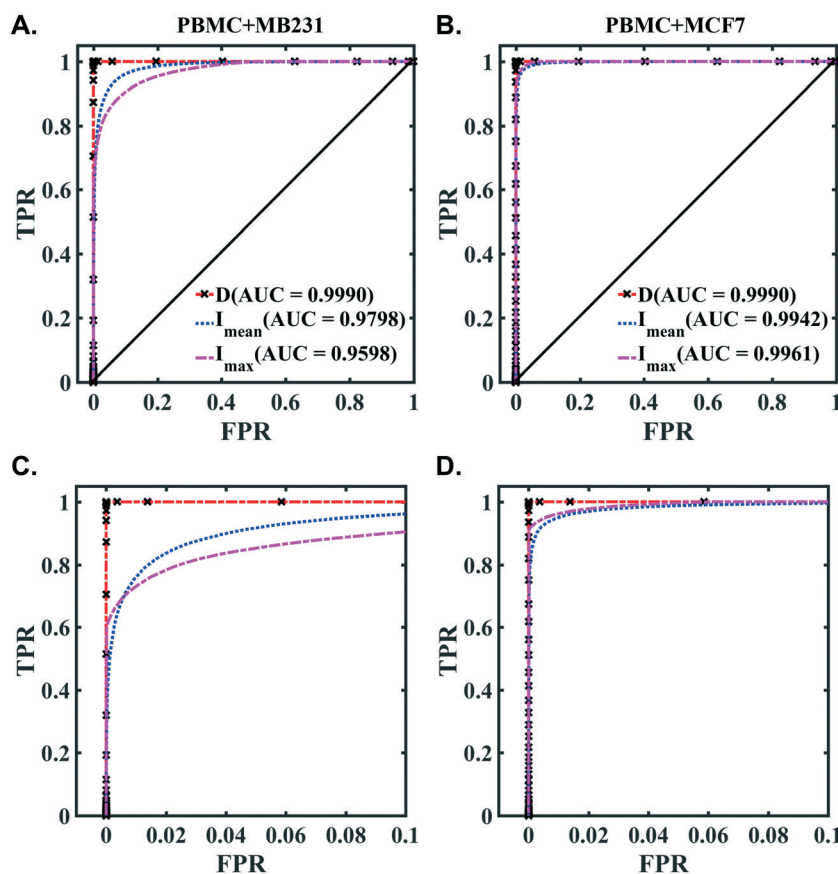


Fig. 5 The receiver operating characteristics (ROC) curve showing the false positive rate (FPR) versus the true positive rate (TPR) with respect to three characteristic metrics: size (D), mean intensity (I_{mean}), and maximum intensity (I_{\max}). The ROC curve is shown for distinguishing (A) PBMC & MDA-MB-231 and (B) PBMC & MCF7 where the line TPR = FPR corresponds to random guessing. For visual clarity the zoomed-in ROC curves to a false positive rate of 0.1 are presented in (C) and (D) corresponding to (A) and (B) respectively.

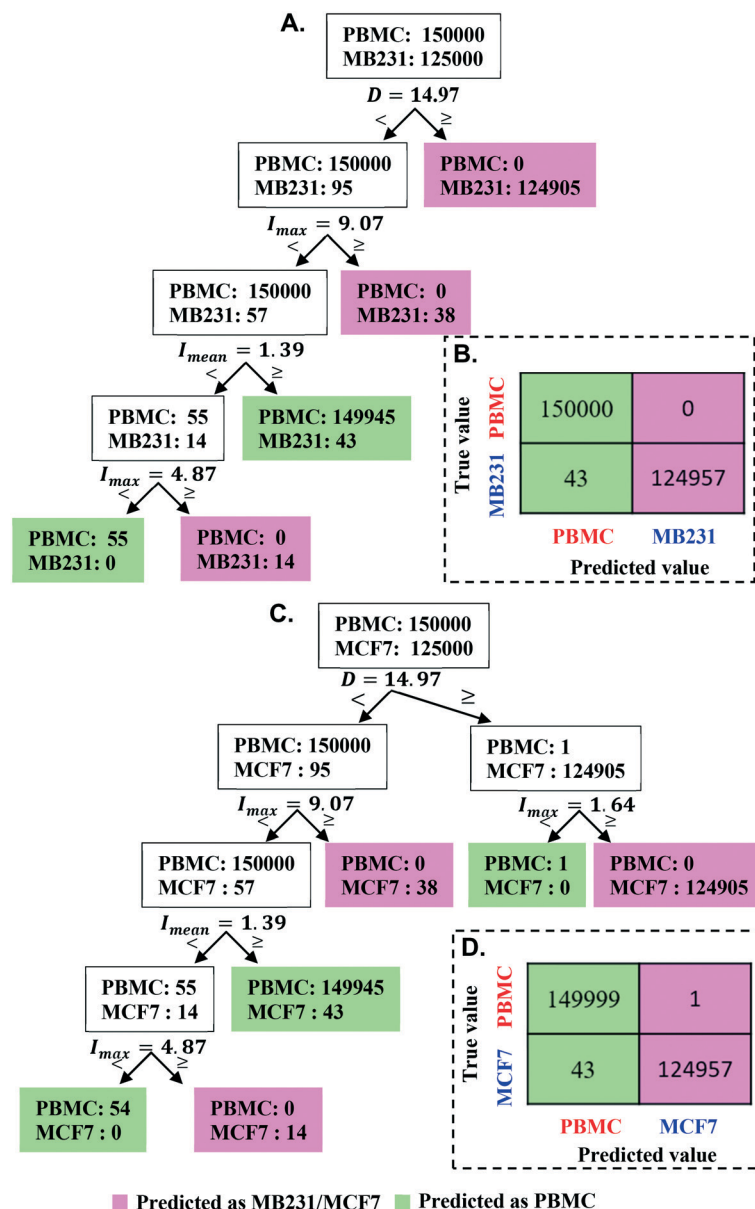


Fig. 6 The decision tree based on the CART-algorithm to develop classifiers using the characteristic metrics of size (D), maximum intensity (I_{\max}) and mean intensity (I_{mean}) to discriminate populations of PBMC & MDA-MB-231(MB231) and PBMC & MCF7. (A) & (B) show the decision tree and the predicted values of PBMC and MB231 cells with respect to their true values. Similarly, (C) & (D) show the decision tree and the predicted values of PBMC and MCF7 cells with respect to their true values.

metrics is necessary for optimal differentiation. We also verified that linear discriminant analysis and support vector machines generated similar improved accuracy over binary discriminants by incorporating all three metrics. In summary, these results suggest the potential for each of the three metrics, D , I_{\max} , and I_{mean} , to support enumeration of tumor cells within a background of blood.

2.4 Identification and enumeration of spiked tumor cells in lysed whole blood

The classification strategies developed above were used to identify breast tumor cells within a background of lysed

blood based on the inline-DHM metrics of size, maximum intensity, and mean intensity. In more detail, samples containing crude ACK Lysing Buffer-processed healthy donor blood cells containing WBCs and residual RBCs at a total cell concentration of 0.45 million per mL were spiked with breast tumor cells (MDA-MB-231 or MCF7) at approximately 10, 50, and 100 tumor cells per mL. Significantly, the blood donor was distinct from the donor used to develop the classifier. In these experiments, each hologram corresponds to measuring approximately 100 cells. Since we acquired 100 holograms per second for 45 s, we processed 4500 holograms and characterized $\approx 450\,000$ cells per spiked sample, or equivalently 10 000 cells per second.

With respect to computational analysis, each hologram was numerically reconstructed and the position, size, and intensity of each cell were determined. Fig. 7A shows the cropped hologram ($500 \times 500 \mu\text{m}^2$) of cells flowing through the channel, from the original hologram of size $1024 \times 1024 \mu\text{m}^2$. The decision classifier developed through training data (Fig. 6) was used to differentiate blood cells from each cancer cell line enabling a 3D reconstruction of the location and inferred identity of the mixed cells within the channel (Fig. 7B). This single snap-shot shows the location of thirty cells classified as PBMCs (red) and two cells classified as MCF7 cells (blue) flowing along the x -direction within the rectangular microfluidic device (Fig. 7B). We note that the laminar nature of flow introduces the complication of counting slower cells multiple times in sequential frames. The multiple counting of cells has been eliminated using the streamline coordinates, y and z , of reconstructed cells. The detailed process of eliminating multiple counts has been reported in our previous work.²⁸

Fig. 7C and D report the number of feed (input) and the identified (output) breast tumor cells, MDA-MB-231 and MCF7 respectively. At a spiked concentration of $C = 0$ tumor cells, 6 cells were identified as false positive out of 450 000 reconstructed lysed blood cells using classifier defined for MDA-MB-231 in Fig. 6A whereas; using the classifier for MCF7 as defined in Fig. 6B, no false positives were identified out of

450 000 reconstructed lysed blood cells. At spiked concentrations targeting $C = 10, 50$, and 100 cells per mL solution, for each breast tumor cell line the numbers of feed (input) cells are in close agreement with those of the identified (output) cells (Fig. 7C and D, ESI† SM1). Differences in exact values are attributed to challenges in making accurate stock solutions due to manual counting errors using a hemocytometer at low concentrations and dilutions of a stock solution⁴⁵ as well as variable cell settling prior to imaging sub fractions of the prepared solutions. That differences between the intended and observed cell number do not vary systematically supports this hypothesis of random error. The low false positive rate cancer cells identified in the PBMC sample was replicated in blood processed from two additional donors (ESI† SM2).

Next, we estimate the limit of detection (LoD) for DHM to fingerprint tumor cells in blood. LoD can be defined as the mean number of tumor cells detected in non-spiked sample $+2 \times$ (standard deviation). Using the data reported in ESI† Table SM2, we find that for MCF-7 cells LoD = 4.33 cells per mL and for MDA-MB231 cells LoD = 9 cells per mL. This LoD is potentially sufficient for DHM to enumerate CTCs in advanced cancer patient blood samples since using the CTC-chip⁴⁵ it was found that in 55 lung cancer patient samples tested, 11 had 5–20 CTCs per mL, 11 had 20–50 CTCs per mL, 11 had 50 CTCs per mL and 22 had more than 100 CTCs

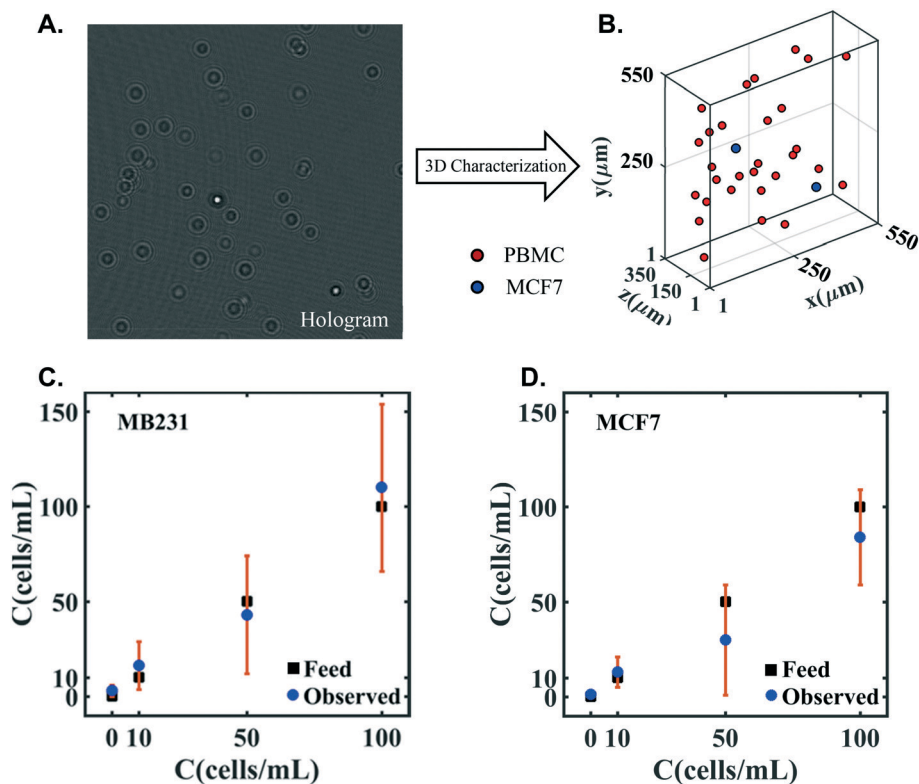


Fig. 7 Identification and enumeration of tumor cells spiked in lysed whole blood. (A) The hologram of lysed blood sample spiked with MCF7 cells, (B) 3D model generated from numerical reconstruction of single hologram in (A). Identification of spiked cells (C) MDA-MB-231 and (D) MCF7 cells at three different concentrations of spiking in the lysed blood populations of 0.45 million per mL of PBMC. The square-black and circular-blue symbols show the concentration of spiked cells (feed) and detected cells (observed) is presented. The concentration of PBMCs is 0.45 million per mL in PBS. Error bars represent the standard deviation of 3 experiments. A ESI† tables (SM1 and SM2) shows the detailed values of each data point.

per mL. Future studies focusing on patient blood samples can provide an actual quantitative estimate of limit of detection of DHM-based label-free identification of CTCs.

3. Discussion

In this work, we have introduced inline-DHM as a label-free imaging platform appropriate for the identification and characterization of cells in bulk flow, with a focus on detecting tumor cells in blood. We have established three suitable metrics, cell diameter, I_{\max} and I_{mean} , for characterizing blood components and tumor cells. We applied machine-learning approaches to identify tumor cells within a background of blood cells. Testing the classifier on the distinct blood sample used for the spiked experiments resulted in, at most, 0.001% false positives (blood cells identified as tumor cells). Below we discuss how our existing approach can be advanced to achieve significantly more throughput and also present avenues for configuring DHM technology for analyzing real CTCs in patient samples.

Advancing current capabilities of DHM

In this study, we typically analyzed ≈ 100 cells per 3D image volume and 4500 holograms, achieving a throughput of 450 000 cells per sample. In the future, it is possible to increase the throughput of cellular analysis to 10^6 – 10^7 cells per sample. The main limiting factors for increasing throughput is the camera system needed to record/store the holograms and the computational time required for numerical reconstruction. In this work, we used a CMOS camera (Phantom v.310) to record at 100 fps and store 4500 holograms per sample. The 16GB RAM available on this camera can be used to store as many as 20 000 holograms, indicating that 2×10^6 cells can be analyzed with our existing hardware. However, the time-consuming step then becomes the computational processing of the holograms. Here, we used a standard desktop computer (3.6 GHz processor, 8 GB RAM) to analyze the 4500 holograms, which took ≈ 7 s per hologram and ≈ 8.75 hours per sample. Rather than a single processor, by pursuing distributed computing, along with optimized reconstruction algorithms, we anticipate the computational analysis time can be reduced significantly. Given that the computational processing can be done off-line and is not labor intensive, our label-free approach outcompetes tedious immunofluorescence staining methods to detect cancer cells in mixed populations.

We acknowledge that there are other digital holographic implementations.^{46–51} We have chosen to implement inline-DHM in the present study due to its relatively simple configuration, straightforward implementation with microfluidic systems and capability to handle large sample volume with reduced computational analysis. In addition, it is easier to obtain x , y and z coordinates of the cells in the imaged sample volume which are used to correlate the cells between successive frames and eliminate multiple counting of cells.

Moving DHM towards analyzing CTCs in cancer patient samples

Looking towards applications targeting patient screening, it is generally accepted that at least 3 mL of patient blood needs to be processed to achieve reliable information about CTCs where whole blood is estimated to contain approximately $4\text{--}5 \times 10^9$ RBCs and $5\text{--}11 \times 10^6$ WBCs per mL. In this study, we have used lysed blood and since the sample injection flow rate is $1400 \mu\text{L min}^{-1}$, the volume processing rate is $23 \mu\text{L s}^{-1}$. Sample preparation involving lysis of RBCs in 3 mL of patient blood will yield $\approx 10^7$ WBCs per mL in 22 mL, which can be imaged by DHM in ≈ 50 minutes @ 100 fps. We note that the injection flow rate or sample processing rate can be increased to beyond what we used in this study, in which case the camera frame rate would need to be increased. This will also lead to reduced image acquisition time.

Rather than lysing blood, non-invasive CTC enrichment strategies can also be pursued in combination with DHM detection. For example, RBCs might be removed through deterministic lateral displacement (DLD) debulking in which fluid under laminar flow regimes is passed through asymmetric micropillar arrays in a microfluidic device.^{52,53} Samples might be further enriched by additionally removing a sub-population of PBMCs through a variety of inertial techniques such as those incorporated into spiral devices using dean flow fractionation (DFF),^{10,54} the Vortex Chip,⁷ and the multi orifice flow fractionation (MOFF) microfluidic device.¹⁴

Using the above enrichment methods, it is useful to estimate the amount of image acquisition that is needed to DHM-process the entire sample volume. Integrating the DFF⁵⁴ method which enriches the sample by 10^9 fold over RBCs and 10^3 fold over WBCs, 3 mL of injected blood sample results in ≈ 25 mL of enriched sample containing 1300 WBCs per mL. Given the sample processing rate is $23 \mu\text{L s}^{-1}$ in this study, we can DHM-image the ≈ 25 mL in ≈ 19 minutes @ 100 fps – which is $3\times$ less time than the lysis method. Processing methods such as the Vortex Chip,⁷ which recover highly enriched samples in small volumes (<1 mL) might be DHM-imaged in <60 seconds.

Finally, in this study we have demonstrated detection of as few as 10 tumor cells per mL at a preliminary false positive rate of 0.001%. We have quantified and reported the low rate of cell line false negatives in table in Fig. 6B (for MCF7) and Fig. 6D (for MDA-MB-231) – both show 43/124957 or 0.034%. The accuracy of detection can be improved by incorporating additional metrics (*e.g.* gradient of intensity) from the data-rich holograms. Such improved metrics should also limit false negatives of patient-derived CTCs as the strong signals exhibited by the two tested cell lines might not extend to patient-derived samples. Thus, the DHM technology has the potential to robustly identify CTCs and classify their subpopulations without destructive processing and labeling of cells.

4. Conclusion

Results presented here analyzing donor blood and cancer cell lines suggest that the combined DHM-derived signatures of

single cell diameters and intensity profiles provide a new and promising metric for differentiating tumor derived cells from background hematopoietic cell types. Using these metrics, inline-DHM is expected to provide rapid, highly accurate, platform-flexible, and label-free discrimination of tumor cells in patient blood. Moving beyond CTC applications, our approach provides a generic label-free method for detecting target cells in mixed populations, which is useful in cytopathology, drug resistance, and identification of rare stem cells.

5. Methods

5.1 Microfluidic device fabrication

The microfluidic channels of width, $w = 1000\ \mu\text{m}$, and height, $h = 350\ \mu\text{m}$, were fabricated using soft lithography.⁵⁵ Negative photoresist (SU-8 2050) were used to make the mold. Polydimethyl siloxane (PDMS) prepolymer and curing agent were mixed in a 10:1 ratio, degassed, poured on the mold and cured for a minimum of two hours at 65 °C. The PDMS replica was cut with a scalpel and peeled. Inlet and outlet reservoirs were defined by punching holes and the channel was irreversibly bonded to a glass slide 25 mm × 75 mm × 1 mm; Fisher) after exposing the bonding surfaces of the PDMS device and glass slide to plasma for 2 minutes.

5.2 DHM sample preparation

For bead validation assays, polystyrene beads (Polyscience Inc., NIST traceable polystyrene beads) and silica beads (Corpuscular Inc., Monodisperse Silica Microspheres) of mean diameters of 8 and 15 μm were used. Beads were diluted into phosphate buffered saline to a final concentration of 0.45 million beads per ml prior to characterization.

For single cell type characterization tumor cell lines MDA-MB-231 (passage 9, purchased from ATCC, Manassas, VA) and MCF-7 (passage 10, provided by Dr. Lauren Gollahon at Texas Tech University) were cultured in DMEM media supplemented by 10% fetal bovine serum (FBS), 1% penicillin–streptomycin solution (Gibco) and 1 nM sodium pyruvate. Prior to DHM imaging, adherent cultured cells were detached by incubating with trypsin/EDTA solution, neutralized with serum and suspended in phosphate buffered saline. Cells were filtered through a 30 μm pre-separation filter (Miltenyi Biotec) and adjusted to the designated concentrations by further dilution with phosphate buffered saline.

Whole human blood was obtained from consenting healthy donors under IRB-approved protocols and processed three days after blood donation. RBCs were characterized as a concentrated subpopulation purified from platelets and white blood cells using Ficoll-Paque with SepMate separation inserts (Stemcell Technologies) as directed by manufacturers. WBCs were isolated from whole blood using ACK Lysing Buffer (Life Technologies) as directed by manufacturer including a secondary lysing step to support more complete RBC removal. Cancer cell lines were cultured on tissue culture polystyrene using standard tissue culture procedures and imaged within one hour after trypsin mediated detach-

ment. Suspensions of cancer cell lines or blood components were filtered through a 30 μm filter and diluted to approximately 0.45 million cells per mL in PBS prior to DHM processing. More than 100 000 cells were processed for each sample.

5.3 Digital holography microscopy setup

Details of our DHM set up are identical to those described in our previous study.²⁸ Briefly, as shown in Fig. 1A the in-line DHM arrangement consists of a laser, a spatial filter and collimator assembly, and an inverted optical microscope (IX-71, Olympus Inc.). A He–Ne laser (10 mW, $\lambda = 0.6328\ \mu\text{m}$, Thorlabs) is used as a light source, operating in continuous wave (CW) mode. The laser beam is filtered and expanded by a spatial filter assembly consisting of a microscope objective (10×, NA = 0.25; Thorlabs) and a pinhole (25 μm diameter). The expanded beam is then collimated using a plano-convex lens (focal length, $f = 100\ \text{mm}$, Thorlabs). The diameter of the collimated beam is approximately 5 mm. This collimated beam of laser light illuminates cells or beads flowing in the microfluidic channel. The flow through the channel is generated by a syringe pump (KD Scientific). The cross-sectional dimensions of the channel are 1000(y) × 350(z) μm^2 . The 2D hologram of cells or beads is generated in the focal plane of the microscope objective ($M = 10\times$, NA = 0.25; Thorlabs) of the optical microscope. The magnified image of the hologram is recorded on a CMOS camera (Phantom v310, Vision Research) at a resolution of 512 × 512 (20 μm per pixel) and 12-bit gray level quantization. The influence of DHM recording parameters on accuracy of determining axial position and scattered intensity are described in our previous work.²⁸

5.4 Data analysis platform

The recorded holograms were transferred to a computer for numerical reconstruction and data analysis. Detailed reconstruction methodology for characterization of particles^{33–35} and of cells is described in our previous work.²⁸ We implemented numerical reconstruction procedure in MATLAB, using a standard desktop computer (Intel(R) Core (TM) i7-4790 @ 3.60GHz, RAM: 8.00GB). The processing time is about 1.94 hours to analyze 1000 holograms.

Author contributions

All authors contributed to the design of the experiments and research. DKS and CCA conducted the experiments and obtained the data. All authors analyzed the data. DKS, CCA and SAV wrote the paper and all authors provided feedback on the manuscript. SAV supervised the project.

Competing financial interests

The authors declare no competing financial interests.

Acknowledgements

Research was supported by Cancer Prevention and Research Institute of Texas (CPRIT) under the grant no. RP140840. Authors thank Dr. Jian Sheng and Dr. Vinodhan Manoharan for useful discussions on the development of digital holography microscopy for cellular characterization as well as Jacqueline Berry for her technical assistance in blood processing.

References

- 1 S. Maheswaran and D. A. Haber, Circulating tumor cells: a window into cancer biology and metastasis, *Curr. Opin. Genet. Dev.*, 2010, **20**, 96–99.
- 2 S. Maheswaran, *et al.*, Detection of mutations in EGFR in circulating lung-cancer cells, *N. Engl. J. Med.*, 2008, **359**, 366–377.
- 3 M. Yu, S. Stott, M. Toner, S. Maheswaran and D. A. Haber, Circulating tumor cells: approaches to isolation and characterization, *J. Cell Biol.*, 2011, **192**, 373–382.
- 4 K. Pantel and M. R. Speicher, The biology of circulating tumor cells, *Oncogene*, 2016, **35**, 1216–1224.
- 5 M. M. Ferreira, V. C. Ramani and S. S. Jeffrey, Circulating tumor cell technologies, *Mol. Oncol.*, 2016, **10**, 374–394, DOI: 10.1016/j.molonc.2016.01.007.
- 6 R. A. Harouaka, M. Nisic and S.-Y. Zheng, Circulating tumor cell enrichment based on physical properties, *J. Lab. Autom.*, 2013, **18**, 455–468.
- 7 J. Che, *et al.*, Classification of large circulating tumor cells isolated with ultra-high throughput microfluidic Vortex technology, *Oncotarget*, 2016, **7**, 12748–12760.
- 8 E. E. van der Toom, J. E. Verdone, M. A. Gorin and K. J. Pienta, Technical challenges in the isolation and analysis of circulating tumor cells, *Oncotarget*, 2016, **7**, 62754–62766.
- 9 E. Reategui, *et al.*, Tunable nanostructured coating for the capture and selective release of viable circulating tumor cells, *Adv. Mater.*, 2015, **27**, 1593–1599, DOI: 10.1002/adma.201404677.
- 10 M. E. Warkiani, *et al.*, Slanted spiral microfluidics for the ultra-fast, label-free isolation of circulating tumor cells, *Lab Chip*, 2014, **14**, 128–137.
- 11 Y. Fang, Label-free drug discovery, *Front. Pharmacol.*, 2014, **5**, 52, DOI: 10.3389/fphar.2014.00052.
- 12 N. Aceto, *et al.*, Circulating tumor cell clusters are oligoclonal precursors of breast cancer metastasis, *Cell*, 2014, **158**, 1110–1122.
- 13 J. Zhang, *et al.*, Fundamentals and applications of inertial microfluidics: a review, *Lab Chip*, 2016, **16**, 10–34.
- 14 H. S. Moon, *et al.*, Continual collection and re-separation of circulating tumor cells from blood using multi-stage multi-orifice flow fractionation, *Biomicrofluidics*, 2013, **7**, 14105.
- 15 J. S. Bagnall, *et al.*, Deformability-based cell selection with downstream immunofluorescence analysis, *Integr. Biol.*, 2016, **8**, 654–664.
- 16 R. Mitra, O. Chao, Y. Urasaki, O. B. Goodman and T. T. Le, Detection of lipid-rich prostate circulating tumour cells with coherent anti-Stokes Raman scattering microscopy, *BMC Cancer*, 2012, **12**, 540.
- 17 S. Shim, *et al.*, Antibody-independent isolation of circulating tumor cells by continuous-flow dielectrophoresis, *Biomicrofluidics*, 2013, **7**, 11807, DOI: 10.1063/1.4774304.
- 18 P. Li, *et al.*, Acoustic separation of circulating tumor cells, *Proc. Natl. Acad. Sci. U. S. A.*, 2015, **112**, 4970–4975.
- 19 U. Schnars and W. Jüptner, Direct recording of holograms by a CCD target and numerical reconstruction, *Appl. Opt.*, 1994, **33**, 179–181, DOI: 10.1364/AO.33.000179.
- 20 J. Sheng, E. Malkiel and J. Katz, Digital holographic microscope for measuring three-dimensional particle distributions and motions, *Appl. Opt.*, 2006, **45**, 3893–3901, DOI: 10.1364/AO.45.003893.
- 21 J. Sheng, E. Malkiel and J. Katz, Using digital holographic microscopy for simultaneous measurements of 3D near wall velocity and wall shear stress in a turbulent boundary layer, *Exp. Fluids*, 2008, **45**, 1023–1035.
- 22 Y.-S. Choi and S.-J. Lee, Three-dimensional volumetric measurement of red blood cell motion using digital holographic microscopy, *Appl. Opt.*, 2009, **48**, 2983–2990, DOI: 10.1364/AO.48.002983.
- 23 T. A. Ooms, R. Lindken and J. Westerweel, Digital holographic microscopy applied to measurement of a flow in a T-shaped micromixer, *Exp. Fluids*, 2009, **47**, 941–955.
- 24 J. Katz and J. Sheng, Applications of Holography in Fluid Mechanics and Particle Dynamics, *Annu. Rev. Fluid Mech.*, 2010, **42**, 531–555.
- 25 L. Tian, N. Loomis, J. A. Domínguez-Caballero and G. Barbastathis, Quantitative measurement of size and three-dimensional position of fast-moving bubbles in air-water mixture flows using digital holography, *Appl. Opt.*, 2010, **49**, 1549–1554.
- 26 F. Dubois and C. Yourassowsky, WO 2013083563 A1, 2013.
- 27 S. Jooris and P. Mathuis, WO 2014044823 A1, 2015.
- 28 D. K. Singh, C. C. Ahrens, W. Li and S. A. Vanapalli, Label-free fingerprinting of tumor cells in bulk flow using inline digital holographic microscopy, *Biomed. Opt. Express*, 2017, **8**, 536–554, DOI: 10.1364/BOE.8.000536.
- 29 M. K. Kim, Principles and techniques of digital holographic microscopy, *J. Photonics Energy*, 2010, 018005.
- 30 J. W. Goodman, *Introduction to Fourier Optics*, McGraw-Hill, 1968.
- 31 T. Kreis, *Handbook of Holographic Interferometry Optical and Digital Methods*, Wiley-VCH Verlag GmbH & Co., 2005.
- 32 Y.-S. Choi and S.-J. Lee, Three-dimensional volumetric measurement of red blood cell motion using digital holographic microscopy, *Appl. Opt.*, 2009, **48**, 2983–2990.
- 33 D. K. Singh and P. K. Panigrahi, Three-dimensional investigation of liquid slug Taylor flow inside a micro-capillary using holographic velocimetry, *Exp. Fluids*, 2015, **56**, 1–15, DOI: 10.1007/s00348-014-1863-9.
- 34 D. K. Singh and P. K. Panigrahi, Automatic threshold technique for holographic particle field characterization, *Appl. Opt.*, 2012, **51**, 3874–3887, DOI: 10.1364/AO.51.003874.

- 35 D. K. Singh and P. K. Panigrahi, Improved digital holographic reconstruction algorithm for depth error reduction and elimination of out-of-focus particles, *Opt. Express*, 2010, **18**, 2426–2448.
- 36 E. M. Zetsche, *et al.*, Imaging-in-Flow: Digital holographic microscopy as a novel tool to detect and classify nanoplanktonic organisms, *Limnol. Oceanogr.: Methods*, 2014, **12**, 757–775.
- 37 D. K. Singh and P. K. Panigrahi, in *Digital Holography and Three-Dimensional Imaging*, DTuC29, Optical Society of America, 2011.
- 38 P. F. Mullaney, M. A. Van Dilla, J. R. Coulter and P. N. Dean, Cell Sizing: A Light Scattering Photometer for Rapid Volume Determination, *Rev. Sci. Instrum.*, 1969, **40**, 1029–1032.
- 39 W. Choi, *et al.*, Tomographic phase microscopy, *Nat. Methods*, 2007, **4**, 717.
- 40 V. P. Maltsev, A. G. Hoekstra and M. A. Yurkin, Optics of White Blood Cells: Optical Models, Simulations, and Experiments, in *Advanced Optical Flow Cytometry: Methods and Disease Diagnoses*, ed. V. V. Tuchin, Wiley-VCH Verlag GmbH & Co. KGaA, Weinheim, Germany, 2011.
- 41 P. Liu, *et al.*, Cell refractive index for cell biology and disease diagnosis: past, present and future, *Lab Chip*, 2016, **16**, 634–644.
- 42 X. Liang, A. Liu, C. Lim, T. Ayi and P. Yap, Determining refractive index of single living cell using an integrated microchip, *Sens. Actuators, A*, 2007, **133**, 349–354.
- 43 V. G. Daniels, P. R. Wheeler and H. G. Burkitt, *Functional histology: A text and colour atlas*, Churchill Livingstone, Edinburgh, 1979.
- 44 X. J. Liang, A. Q. Liu, C. S. Lim, T. C. Ayi and P. H. Yap, Determining refractive index of single living cell using an integrated microchip, *Sens. Actuators, A*, 2007, **133**, 349–354.
- 45 Y. Zhao, P. G. Schiro, J. S. Kuo, L. Ng and D. T. Chiu, Method for the accurate preparation of cell-spiking standards, *Anal. Chem.*, 2008, **81**, 1285–1290.
- 46 X. Quan, K. Nitta, O. Matoba, P. Xia and Y. Awatsuji, Phase and fluorescence imaging by combination of digital holographic microscopy and fluorescence microscopy, *Opt. Rev.*, 2015, **22**, 349–353.
- 47 K. Jaferzadeh and I. Moon, Quantitative investigation of red blood cell three-dimensional geometric and chemical changes in the storage lesion using digital holographic microscopy, *J. Biomed. Opt.*, 2015, **20**, 111218.
- 48 Y. Sung, *et al.*, Three-Dimensional Holographic Refractive-Index Measurement of Continuously Flowing Cells in a Microfluidic Channel, *Phys. Rev. Appl.*, 2014, **1**, 014002.
- 49 K. Lee, *et al.*, Quantitative phase imaging techniques for the study of cell pathophysiology: from principles to applications, *Sensors*, 2013, **13**, 4170–4191, DOI: 10.3390/s130404170.
- 50 B. Kemper, *et al.*, Integral refractive index determination of living suspension cells by multifocus digital holographic phase contrast microscopy, *J. Biomed. Opt.*, 2007, **12**, 054009, DOI: 10.1117/1.2798639.
- 51 B. Rappaz, *et al.*, Measurement of the integral refractive index and dynamic cell morphometry of living cells with digital holographic microscopy, *Opt. Express*, 2005, **13**, 9361–9373.
- 52 L. R. Huang, E. C. Cox, R. H. Austin and J. C. Sturm, Continuous particle separation through deterministic lateral displacement, *Science*, 2004, **304**, 987–990.
- 53 E. Ozkumur, *et al.*, Inertial focusing for tumor antigen-dependent and-independent sorting of rare circulating tumor cells, *Sci. Transl. Med.*, 2013, **5**, 179ra147.
- 54 H. W. Hou, *et al.*, Isolation and retrieval of circulating tumor cells using centrifugal forces, *Sci. Rep.*, 2013, **3**, 1259.
- 55 D. C. Duffy, J. C. McDonald, O. J. Schueller and G. M. Whitesides, Rapid prototyping of microfluidic systems in poly (dimethylsiloxane), *Anal. Chem.*, 1998, **70**, 4974–4984.